A time-resolved paleomagnetic record of Main Group pallasites: Evidence for a Psyche-like parent body

Claire I. O. Nichols[a,b], James F.J. Bryson[b], Rory D. Cottrell[c] Roger R. Fu[d], Richard J. Harrison[e], Julia Herrero-Albillos[f,g] , Florian Kronast[h], John A. Tarduno[c], Benjamin P. Weiss[a]

[a] Department of Earth, Atmospheric and Planetary Sciences, Massachusetts Insitute of Technology, Cambridge, MA 02139, USA
[b] Department of Earth Sciences, University of Oxford, Oxford, OX1 3AN, UK
[c] Department of Earth and Environmental Sciences, University of Rochester, NY 14627, USA
[d] Department of Earth and Planetary Sciences, Harvard University, Cambridge MA, USA
[e] Department of Earth Sciences, University of Cambridge, Cambridge, CB2 3EQ, UK
[f] Departamento de Ciencia y Tecnología de Materiales y Fluidos, Universidad de Zaragoza, Spain
[g] Instituto de Nanociencia y Materiales de Aragón (INMA), CSIC—Universidad de Zaragoza, Zaragoza 50009, Spain
[h] Helmholtz-Zentrum Berlin für Materialien und Energie, Albert-Einstein-Strasse 15, 12489 Berlin, Germany

Abstract

Several paleomagnetic studies have been conducted on five main group pallasites: Brenham, Marjalahti, Springwater, Imilac and Esquel. These pallasites have distinct cooling histories, meaning that their paleomagnetic records may have been acquired at different times during the thermal evolution of their parent body. Here we compile new and existing data to present the most complete time-resolved paleomagnetic record for a planetesimal, which includes a period of quiescence prior to core solidification as well as dynamo activity generated by compositional convection during core solidification. We present new paleomagnetic data for the Springwater pallasite, which constrains the timing of core solidification. Our results suggest that in order to generate the observed strong paleointensities ($65 - 95\ \mu$T), the pallasites must have been relatively close to the dynamo source. Our thermal and dynamo models predict that the main group pallasites originate from a planetesimal with a large core (> 200 km) and a thin mantle (< 70 km). The density of our model large-cored planetesimals is similar to the predicted density of the asteroid (16) Psyche. We therefore suggest that it is plausible that the main group pallasites originated from a Psyche-like parent body.

Plain Language Summary: We have studied 5 pallasite meteorites which are comprised of a green mineral called olivine surrounded by iron-nickel metal. These meteorites are all thought to originate from the same parent asteroid. We have measured the magnetism of these meteorites, and recovered information about the magnetic fields they experienced when they initially formed and cooled. Our magnetic measurements show that the parent asteroid generated its own magnetic field, suggesting that the asteroid had a metallic core which was vigorously convecting. We find that our results are best explained by the parent asteroid having a very large metal core and a thin rocky shell. This is very similar to the proposed structure of the asteroid (16) Psyche from astronomical observations. We therefore suggest that the pallasite meteorites may have come from an asteroid similar to Psyche. This is a timely observation, since a spacecraft is due to orbit Psyche for the first time in 2026 allowing our hypothesis to be tested.

1 Introduction

The main group (MG) pallasites are all thought to originate from the same planetesimal (Greenwood et al., 2006). Temporal variations in core dynamo activity on this parent asteroid have been shown by several paleomagnetic studies. For instance, Tarduno et al. (2012) found the first evidence for dynamo activity recorded by magnetic inclusions in olivine crystals from the Imilac and Esquel pallasites. This observation was supported by a paleomagnetic study of the cloudy zone in the Imilac and Esquel pallasites (Bryson et al., 2015). Both studies retrieved paloeintensites of ~ 100 μT, interpreted as evidence for an active dynamo $\sim 140 - 240$ Myr after parent body accretion. An active thermal dynamo is predicted to have only lasted for a maximum of ~ 40 Myr after accretion (Elkins-Tanton et al., 2011; Bryson et al., 2019b; Dodds et al., 2021). Therefore this measured magnetic remanence has instead been attributed to compositional convection resulting from core solidification. A subsequent paleomagnetic study of the cloudy zone in the Marjalahti and Brenham pallasites found no evidence of an active dynamo $\sim 100 - 120$ Myr after accretion (Nichols et al., 2016). Dynamo initiation and the onset of core solidification was therefore predicted to occur between the time at which Brenham

and Marjalahti, and subsequently Imilac and Esquel acquired their paleomagnetic records.

Paleomagnetic signals are recorded by two mechanisms in pallasites. Magnetic inclusions of taenite (with 50 – 55 wt%Ni) within the olivine crystals acquire a thermal remanent magnetization (TRM) upon cooling below their blocking temperature between 360 – 500 °C (Tarduno et al., 2012). The cloudy zone (an FeNi microstructure that forms as part of the Widmanstätten pattern in meteoritic metal) acquires a chemical transformation remanent magnetization (CTRM) when tetrataenite ordering occurs below 320 °C (Einsle et al., 2018). Therefore the timing of remanence acquisition for both of these mechanisms is dependent upon cooling rate; slower-cooled pallasites will record paleomagnetic signals at a later time than fast-cooled pallasites.

Here we investigate paleomagnetic signals recorded by the Springwater pallasite cloudy zone using X-ray photoemission electron microscopy (X-PEEM) and reassess the signals recorded by the cloudy zones of Brenham, Marjalahti, Imilac and Esquel with the aim of better understanding this dynamo record and its implications for the thermal history and structure of the parent body. Springwater has an intermediate cooling rate among these five pallasites, so has the potential to capture the onset of core solidification and the initiation of a compositionally driven dynamo. We also assess the rock magnetic and paleomagnetic behaviour of magnetic inclusions in olivines from the Imilac and Springwater pallasites in an attempt to reconcile paleointensity estimates from X-PEEM with those measured using more traditional paleomagnetic techniques (e.g., the Thellier-Thellier method).

Previous studies assumed the MG pallasite parent body had a radius of 200 km and a core with radius 100 km in order for the core to be at least partially molten when Imilac and Esquel acquired a record of the dynamo (Tarduno et al., 2012; Bryson et al., 2015; Nichols et al., 2016). They also assumed that the dynamo was generated by the outward solidification of an inner core (Nimmo, 2009) and that the core contained 31 wt% sulfur and therefore solidified at the FeS eutectic (Ehlers, 1972). Here we consider a range of sulfur compositions and their effect on the timing of core solidification. Given the small size of the planetesimal, we also consider nucleation at the core-mantle boundary and inward core solidification (Williams, 2009) and the

impact of this on dynamo generation.

The pallasites have an enigmatic formation history. They have commonly been interpreted to represent the core-mantle boundary, but this has been questioned given their paleomagnetic record of the dynamo, which suggests they must be at a much lower temperature than the molten core (Tarduno et al., 2012; Bryson et al., 2015; Nichols et al., 2016; Mckibbin et al., 2019). In addition, their varied cooling rates have been used to argue that they formed at a variety of depths in a chaotic asteroid reassembled after impact (Yang et al., 2010). Most recently, it has been suggested that the pallasites could form on a mantle-stripped metallic asteroid, such as asteroid (16) Psyche (Elkins-Tanton et al., 2020). This would resolve the discrepancy between shallow and deep origins for the pallasites, if they originate in the middle of thin mantle that is a short distance from the core-mantle boundary. To resolve the pallasite controversy, Tarduno et al. (2012) suggested an impact whereby dykes from the impactor core penetrated into the parent body mantle. Alternatively, Johnson et al. (2019) recently suggested a mechanism for pallasite formation by which sulfur-rich metallic melts at the core-mantle boundary penetrate a shallow overlying mafic mantle. These authors also suggest the paleomagnetic record of the pallasites may be consistent with a dynamo driven by inward core solidification (Scheinberg et al., 2016; Neufeld et al., 2019).

Here, we present the most complete paleomagnetic record yet of the MG pallasite parent body. We report a new X-PEEM paleointensity for the Springwater pallasite cloudy zone and compile previous paleointensity measurements of the cloudy zone and olivine inclusions in the Brenham, Marjalahti, Imilac and Esquel pallasites. We discuss the implications for the size, internal structure and nature of core solidification on the parent body planetesimal. We argue that the pallasites may originate from a parent body similar to the metallic asteroid (16) Psyche and could originate from within a thin mantle above, but closer to, the core-mantle boundary. The strength and longevity of the pallasite paleomagnetic record suggests a dynamo driven by inward core solidification.

2 Samples and Methods

2.1 X-ray photoemission electron microscopy of the cloudy zone

2.1.1 Sample preparation

A sample of Springwater (BM 1959,1017) was borrowed from the Natural History Museum, London. A 5 × 5 mm section was cut using a tile saw and thinned using a lapping wheel in the presence of water to prevent heating. The sample was then polished with diamond paste grade $9 - 0.25$ μm. The sample was etched for ~ 30 s with nital (2% nitric acid in ethanol) to reveal the FeNi microstructures and was examined using reflected light microscopy to ensure there was no evidence of terrestrial weathering or shock. The sample was then repolished and sputtered for 10 hours at 1.2 keV, 12 hours at 0.8 keV and 1.5 hours at 0.4 keV using a focussed Ar-ion beam under ultra-high vacuum (pressure $< 1.5 \times 10^{-5}$ mbar) to remove any oxidation and surface magnetisation induced by polishing and to minimise surface topography due to differential etching. The sample was kept in vacuum between sputtering and measuring (measuring pressure $< 1.0 \times 10^{-8}$ mbar).

2.1.2 Experimental method

X-PEEM measurements were performed at the SPEEM UE49 beamline, BESSY II, Berlin (Kronast et al., 2010). A beam of monochromatic X-rays was focussed at 16° to the sample surface, exciting secondary photoelectrons from the top ~ 5 nm of the sample surface. The X-rays were tuned to the Fe L_3 edge (~ 707 eV) and linearly polarized to acquire compositional images. Images of magnetization were acquired using X-ray magnetic circular dichroism (XMCD). Images were acquired with a 10 μm field of view. 160 images were collected (80 for each polarization) with an exposure time of 2 s, and then averaged. Averaged images were also corrected for intensity drift due to minor sample charging (see Section S1.1.1).

The X-PEEM technique has been further developed from previous experiments that measured only one magnetization component (Bryson et al., 2014, 2015; Nichols et al., 2016; **?**). We imaged Springwater using the three rotation approach outlined by Bryson et al. (2019a)

which enables the full vector magnetization to be measured. Once the length of the tetrataenite rim-cloudy zone interface had been imaged, the sample was rotated 109° and the same interface was remeasured; the sample was then rotated 120° and remeasured, resulting in three data sets at different angles relative to the X-ray beam. We collected 12, 8 and 7 averaged and corrected images for rotations 1, 2 and 3, respectively.

2.1.3 Paleointensity estimates

The magnitude and direction of the paleomagnetic field recorded by the Springwater cloudy zone was determined following the method outlined by Bryson et al. (2019a). The mean XMCD intensities in each of the three measured orientations (I_1, I_2 and I_3), were used to reconstruct the 3D vector representing the paleomagnetic field at the time of remanence acquisition.

$$I_1 \approx \frac{M_s V}{6k_B T_0}((I_{-x}-I_x)B_x+(I_{-y}-I_y)B_y+(I_{-z}-I_z)B_z)+\frac{1}{6}(I_x+I_{-x}+I_y+I_{-y}+I_z+I_{-z}) \quad (1)$$

$$I_2 \approx \frac{M_s V}{6k_B T_0}((I'_{-x}-I'_x)B_x+(I'_{-y}-I'_y)B_y+(I'_{-z}-I'_z)B_z)+\frac{1}{6}(I'_x+I'_{-x}+I'_y+I'_{-y}+I'_z+I'_{-z}) \quad (2)$$

$$I_3 \approx \frac{M_s V}{6k_B T_0}((I''_{-x}-I''_x)B_x+(I''_{-y}-I''_y)B_y+(I''_{-z}-I''_z)B_z)+\frac{1}{6}(I''_x+I''_{-x}+I''_y+I''_{-y}+I''_z+I''_{-z}) \quad (3)$$

where M_s is the saturation magnetization of tetrataenite (1.12×10^6 Am^{-1}), V is the volume of tetrataenite islands at the time of remanence acquisition, which we take to be 78% of their present day size (Maurel et al., 2019), k_B is the Boltzmann constant, and T_0 is the tetrataenite formation temperature (593 K). The domains in the tetrataenite rim correspond to the XMCD intensities of the orthogonal easy axes I_x, I_{-x}, I_y, I_{-y}, I_z and I_{-z} (Table S3). Although the tetrataenite rim intensities do not directly correspond to one another in different rotations (i.e.,

we did not measure the exact same field of view for each rotation), the uncertainty in how the intensities change with rotation has a negligible effect (< 1 μT) on the calculated paleointensity.

Previously calculated paleointensities for the pallasites (Bryson et al., 2015; Nichols et al., 2016) are also reassessed here. Since these estimates were based on one measurement orientation, they represent lower limits on the paleointensity, since it is unknown how the paleofield vector relates to the measurement direction. If the paleomagnetic field direction is parallel to the measurement direction, 100% of the paleointensity is recovered, whereas if the field is perpendicular to the measurement direction, 0% of the paleointensity is recovered. The recovered paleointensity (I_{rec}) is proportional to the true paleointensity of the natural remanent magnetization (I_{NRM}) depending on the angle, θ, between the measurement direction and the paleofield vector:

$$I_{rec} = I_{NRM} \sin\theta \tag{4}$$

We calculated the 95% confidence for I_{NRM} by bootstrapping over all possible values of θ. We sampled 100,000 values of θ distributed evenly over a sphere for the measured values of I_{rec} for Brenham, Marjalahti, Imilac and Esquel. We recovered one-tailed distribution of values for I_{NRM} for each sample. Details of the bootstrapping method are given in the supplementary material S1.1.2.

2.2 Paleomagnetism and rock magnetism of olivine inclusions

2.2.1 Sample preparation

Samples of Springwater were borrowed from the American Museum of Natural History (SW) and the Bowers Q.D. Collection, Harvard Museum of Natural History. A sample of Imilac (IM) was purchased from the meteorite collector *'Meteorite Madness'*. A summary of the samples used in this study and the associated preparation and experimental techniques is shown in Table 1. Samples were selected following the same protocol as Tarduno et al. (2012); regions of gem-quality olivines showing no visible inclusions were preferentially sampled. Gem quality olivines

are identified by concoidal fracture, green colouration (rather than orange, which suggests alteration) and a high degree of translucency. Gem-like olivines $2 - 3$ mm in diameter from the Esquel and Imilac pallasites, sampled > 5 mm from the meteorite edge and several mm from the metal-olivine contact were found to have recoverable natural remanent magnetization (NRM) that was replicable within and between meteorite samples (2 from each meteorite). The success rate from the sampled olivines was 50% if the NRM was of order $10^{-9} - 10^{-10}$ Am^2 (only 15% of specimens analysed). We therefore also preferentially selected samples with NRM moments of this magnitude.

Sample name	Pallasite	Loaned from	Sample preparation	Experimental methods
BM 1959,1017	Springwater	Natural History Museum, London	Polishing, etching and sputtering of metal	X-PEEM
SWH	Springwater	Harvard Museum of Natural History	Diamond wire saw used to isolate oriented olivine cubes	AF demagnetization, IZZI Thellier (controlled-atmosphere furnace), SEM
SWR	Springwater	Harvard Museum of Natural History	Copper hammer/chisel used to 'pop' entire olivines, then soaked in HCl acid	IZZI Thellier (CO_2 laser heating)
SW	Springwater	American Museum of Natural History	Diamond wire saw used to isolate oriented olivine cubes	AF demagnetization
IM	Imilac	Meteorite Madness	Diamond wire saw used to isolate oriented olivine cubes	AF demagnetization, IZZI Thellier (controlled-atmosphere furnace), SEM, QDM

Table 1: Summary of the samples, preparation techniques and experimental methods used in this study. The first column lists the sample name used in this manuscript, the second column lists the pallasite studied, the third column lists the origin of the sample, the fourth column lists how the sample was prepared, the fifth column lists the experimental methods used.

The sample of Springwater from the Harvard Museum of Natural History (SWH) was a large slab (weight $\sim$ 250 g, thickness $\sim$ 1 cm) (Figure S5a). A small ($\sim$5 cm diameter) section was removed from one corner of the slab using an Buehler IsoMet® low speed saw (Figure S5b). All further sampling was carried out using a well precision diamond wire saw at the MIT Paleomagnetism Laboratory. Cutting took place in a magnetically-shielded clean room (DC field $<$ 200 nT), and the saw was thoroughly cleaned between sampling. Mutually oriented samples with a diameter of $\sim 1 - 5$ mm were prepared (Figure S5c). Samples were photographed before and after cutting in order to maintain orientation. Samples were mounted on 2.5 cm diameter quartz glass discs using a minimal quantity of cyanoacrylate cement (Figure S5d). Quartz discs were cleaned and alternating field (AF) demagnetised until they had a moment $< 1 \times 10^{-11}$ Am^2.

A second piece of the Springwater sample from the Harvard Museum of Natural History (SWR) was removed using an ASC Scientific Dual Bladed Rock Saw. Samples were polished using 1 μm Buehler alumina powder to remove the thin layer of epoxy protecting the sample surface. Olivines were then extracted using a small copper hammer and chisel at the Rochester Paleomagnetism and Rock Magnetism Laboratory. The boundary between each olivine and the FeNi matrix was gently tapped until the olivine 'popped' out (Figure S6a). Given the considerable time needed to prepare oriented specimens following methods of Tarduno et al. (2012) unoriented samples were prepared for analysis. Extracted olivines were subsequently soaked in 1 molar HCl acid for $\sim$ 12 hours to remove any surface contamination (Figure S6b). The NRM of olivine samples dropped by up to two orders of magnitude after acid treatment due to removal of alteration at the olivine-metal contact. Once the olivines had been soaked in acid, they were washed in deionised water and examined using a reflected light microscope. Any further obvious surface contamination was removed using a hand-held Dremmel drill. Samples were then mounted in a 1 mm^3 fused quartz box, the magnetic moment of which was measured prior to mounting (Figure S6c). Where possible, samples were wedged in the box with no adhesion, but otherwise a small amount of demagnetised OMEGA® cement, or sodium silicate was used to fix the sample in place.

2.2.2 Alternating field (AF) demagnetization

Experiments were carried out on subsamples of Springwater (SW and SWH) and Imilac (IM) at the MIT Paleomagnetic Laboratory using a 2G Enterprises superconducting rock magnetometer. The magnetometer is shielded within a room made of permalloy and the ambient is $<$ 200 nT for DC fields and $<$ 40 nT for AC fields. NRMs were removed by three axis AF demagnetization in steps of 0.5 mT up to 25 mT, steps of 1 mT up to 95 mT and then steps of 1.5 mT up to 145 mT. The magnetic moment was measured after each AF step and the three orthogonal measurements then averaged to correct for any gyroscopic remanent magnetization (GRM) (Garrick-Bethell et al., 2009; Tikoo et al., 2012). Two samples (SW1Aa and SW3Bb) were further demagnetised manually up to 420 mT in steps of 7.5 mT to test for higher

coercivity components.

Paleointensity estimates were made by comparing the demagnetisation of an NRM to either that of an anhysteretic remanent magnetization (ARM) or an isothermal remanent magnetization (IRM). Samples were given ARMs of 50 μT, 100 μT and 300 μT in an AC field of 260 mT and subsequently AF demagnetised up to 145 mT. Paleointensity estimates were calculated for high coercivity ($>$ 5 mT) components (Figure S9a). The TRM equivalent paleointensity was calculated using

$$I_{ARM} = \frac{\Delta NRM}{\Delta ARM} \cdot \frac{B_{lab}}{f} \tag{5}$$

where ΔNRM and ΔARM are the change in NRM and ARM between demagnetisation steps. B_{lab} is the DC bias field, f is the TRM/ARM ratio which is taken to be $f = 1.34$ because the paleomagnetic carriers in pallaiste olivines are FeNi metal (Stephenson and Collinson, 1974; Gattacceca and Rochette, 2004; Tikoo et al., 2014).

TRM equivalent paleointensities were also determined by comparing AF demagnetization of the NRM to that of a 400 mT IRM for samples SW1Aa, SW1Ab and SWH1frag. Paleointensities were determined using

$$I_{IRM} = \frac{\Delta NRM}{\Delta IRM} \cdot a \tag{6}$$

where ΔNRM and ΔIRM are the change in ARM and IRM between demagnetisation steps, and $a \sim 3000$ μT is a calibration constant, inversely proportional to the TRM / IRM ratio (Stephenson and Collinson, 1974; Gattacceca and Rochette, 2004). It should be noted that this calibration was measured for magnetite, although a similar trend has been observed for FeNi carriers (Fuller and Cisowski, 1987). The uncertainty in paleointensities estimated using this method may be large depending on the exact composition of FeNi carriers and grain size, as well as more fundamental questions of whether demagnetization characteristics of TRM (unblocking temperatures) are adequately represented by ARM or IRM demagnetizations (which reflect magnetic coercivities). We therefore only use calculated paleointensities to assess whether

samples acquired remanence in the presence or absence of a dynamo field.

2.2.3 Controlled atmosphere Thellier-Thellier experiment

Samples of Springwater (SWH) and Imilac (IM) were heated in a ASC Scientific TS-48SC thermal demagnetization oven (internal field < 20 nT) in the MIT Paleomagnetic Laboratory. Samples were heated in a controlled H_2–CO_2 atmosphere as described by Suavet et al. (2014). Samples were held at an oxygen fugacity of IW-2 where IW is the iron-wüstite buffer (Holmes and Arculus, 1982; Brett and Sato, 1984) using H_2–CO_2 gas mixing. We followed the in-field, zero-field, zero-field, in-field (IZZI) protocol (Tauxe and Staudigel, 2004) and heated samples in steps of $25 - 50$ °C from $100 - 500$ °C. Samples were held at each temperature for 20 minutes and took $\sim 10 - 20$ minutes to reach temperature, and < 30 minutes to cool back to room temperature. Partial thermal remanent magnetization (pTRM) checks (Coe et al., 1978) were carried out at 150 °C, 250 °C, 325 °C and 400 °C. For in-field and pTRM check steps, an applied laboratory field of 100 μT was used.

2.2.4 Laser heated IZZI Thellier-Thellier experiment

Samples of Springwater (SWR) were heated using a CO_2 laser in the University of Rochester Paleomagnetism and Rock Magnetism Laboratory in a three-layered shielded room with an ambient field of < 200 nT. The power of the laser was calibrated to temperature using a thermocouple before measuring the samples. Each heating step took < 5 minutes. Approximately 90 s were needed to reach temperature, and the temperature was held for 90 s. The "cooling time" before measurement was $90 - 120$ s, but because of the very small thermal mass of the sample, cooling from high temperature occurs much more rapidly than this duration (O'Brien et al., 2020). Samples were heated and cooled in a magnetically shielded tube. The tube contained a coil so that laboratory fields could also be applied during heating. Both Thellier-Thellier experiments following the IZZI protocol and thermal demagnetisation experiments in the absence of a laboratory field were conducted (Tauxe and Staudigel, 2004; Tarduno et al., 2012). All experiments were conducted using the small-bore (6.3 mm) ultra-high sensitive 3-

component DC WSGI SQUID magnetometer. An applied laboratory field of 60 μT was used for in-field steps.

Samples were initially heated in three large temperature steps to 100 °C, 210 °C and 290 °C to minimise heating times and the chance of alteration at low temperature steps. Between 300 °C and 700 °C samples were heated in temperature steps of 10 – 20 °C.

2.3 Asteroid thermal modelling

We follow a similar approach to Bryson et al. (2015) and assume that the pallasite parent body is spherically symmetric and cools via conduction alone. For the thermal evolution of the mantle, we iteratively solve

$$T_r^t = \kappa \delta t \left(\frac{1}{r \delta r} \left(T_{r+\delta r}^{t-\delta t} - T_{r-\delta r}^{t-\delta t} \right) + \frac{1}{\delta r^2} \left(T_{r+\delta r}^{t-\delta t} - 2T_r^{t-\delta t} + T_{r-\delta r}^{t-\delta t} \right) \right) + T_r^{t-\delta t} \tag{7}$$

where r is the radial distance from the centre of the body, δr is the incremental distance which we set as 1 km, t is time since accretion, δt is the incremental time-step, T_r^t is the temperature of the body at a given radial distance and time and κ is the mantle thermal diffusivity. The surface temperature is fixed at 250 K, and the entire asteroid initially has a temperature of 1600 K, which is approximately the silicate solidus. A summary of the parameters used in our calculations is given in Table 2.

2.3.1 Outward growth of a solid inner core

For nucleation and growth of a solid inner core, we assume the core is isothermal throughout asteroid cooling. For each time-step the entire core cools by:

$$\Delta T = \frac{3 k_m \frac{\delta T}{\delta r}|_{r_c} \delta t}{\rho_c C_p r_c} \tag{8}$$

where k_m is the mantle thermal conductivity, ρ_c is the core density, C_p is the core heat capacity and r_c is the core radius. We allow the core radius to vary from 40 – 60% of the parent body radius.

To model the concentric outward growth of the solid inner core, we follow the model described by Nimmo (2009). The inner core spontaneously nucleates with a radius of 1 km. Its subsequent growth is given by:

$$\frac{\delta r_i}{\delta t} \approx \frac{D^2}{2T_c f r_c(\Delta - 1)} \frac{\delta T_c}{\delta t} \tag{9}$$

where $D = \sqrt{\frac{3C_p}{2\pi\alpha\rho_c G}}$ and is the scale height of convection, α is the thermal expansivity and G is the gravitational constant, T_c is the temperature at the core-mantle boundary, f is the fraction of core that has solidified, where $r_i = f r_c$ and $\Delta = \frac{\delta T_m}{\delta P}\frac{\rho C_p}{\alpha T_i}$ is the relative slope of the solidus to the adiabat ($\Delta > 1$ for inner core solidification). The cooling rate is taken from our thermal model for the pallasite parent body at the core-mantle boundary. When the core cools to the FeS eutectic (1200 K) it remains isothermal until it is entirely solid. We terminate the model when the core is fully solidified, dictated by the total heat extracted across the core mantle boundary equalling the latent heat of the core:

$$Q_{cmb} = 4\pi r_c^2 k_m \frac{\delta T}{\delta r}\Big|_{r_c} = \frac{4}{3}\pi r_c^3 \rho_c L_c \tag{10}$$

where Q_{cmb} is the core mantle boundary heat flux and L_c is the latent heat of core solidification. $\frac{\delta T}{\delta r}\Big|_{r_c}$ was calculated at each time step by taking the difference between the temperature directly above and below the core-mantle boundary. The extracted heat is summed over each subsequent time step until it exceeds the latent heat of the core.

2.3.2 Inward growth of a solid outer core

For concentric inward growth of the core beginning at the core-mantle boundary, we follow the approach of Scheinberg et al. (2016). We assume that the core begins to solidify at the core-mantle boundary when its liquidus temperature is reached. The core is held at the liquidus temperature until a shell (r_{shell}) of 1 km thickness has solidified at the top of the core. The

subsequent thermal evolution of the core is governed by:

$$Q_{ocb} = \frac{4}{3}\pi \left(r_{oc}^3 - (r_{oc} - r_{shell})^3\right) \rho_c L_c \tag{11}$$

where Q_{ocb} is the heat flux across and r_{oc} is the radius of the solid-outer-core liquid-inner-core boundary. The solid outer core and the mantle continue to lose heat via conduction, driving further solidification of the core. When the inner core reaches the eutectic temperature (1200 K) the core is held at this temperature throughout the remaining solidification. Solidification is complete when the cumulative heat flux exceeds the latent heat of the core:

$$Q_{ocb} = \frac{4}{3}\pi r_{ic}^3 \rho_c L_c \tag{12}$$

2.3.3 The influence of sulfur content on core solidification

The core begins to solidify when it reaches the FeS liquidus temperature, which we vary from 1200 – 1590 K corresponding to 18 – 31 wt% S (Ehlers, 1972). We assume that the core is entirely liquid and the mantle is solid when the asteroid differentiates, and therefore the highest liquidus temperature of the core must be below the silicate solidus temperature (1600 K), which corresponds to 18 wt% S. It is assumed that all the sulfur remains in the liquid part of the core and the sulfur content of the liquid core increases by:

$$X_{S_{liq}} = \frac{r_c^3}{r_{liq}^3} X_{S_o} \tag{13}$$

where $X_{S_{liq}}$ is the sulfur content of the liquid part of the core, X_{S_o} is the initial sulfur content of the core, and r_{liq} is the radius of the liquid part of the core. This causes a decrease in the liquidus temperature as core solidification progresses until the FeS eutectic is reached.

2.3.4 The depth of the pallasites within the parent body

The depths of the pallasites within the parent body were calculated based on their cooling rates (Table 4) which were determined at a temperature of 800 K (Yang et al., 2010). We use the

800 K isotherm to find the depth at which each of these cooling rates is met (Bryson et al., 2015). These depths were then interpolated along the 593 K isotherm to find the time at which tetrataenite ordered in each pallasite cooled and remanence was acquired. For the pallasite olivines measured by Tarduno et al. (2012), the depths of the Imilac and Esquel pallasites were interpolated along the 633 K contour, which corresponds to the thermal blocking temperature for taenite with 50 – 55 wt% Ni.

2.4 Asteroid magnetic field generation

2.4.1 A dynamo driven by inner core growth

For outward solidification of a core, the mechanism of dynamo generation via compositional convection is well understood. For this mode of core solidifcation, we calculated the temporal evolution of a dynamo for each of our thermal models. The buoyancy flux, Q_b, generated by core solidification was calculated following Christensen and Aubert (2006) and Aubert et al. (2009):

$$Q_b = \frac{2\pi r_c f \Delta\rho D^2}{T_c(\Delta - 1)} \frac{\delta T_c}{\delta t} \tag{14}$$

which can be used to calculate the Rayleigh number:

$$Ra_Q = \frac{G Q_b}{4\pi\Omega^3 d^4} \tag{15}$$

where Ω is the rotational frequency of the planetesimal and d is the thickness of the molten part of the core. We assume a fairly rapid rotational frequency consistent with that observed for the asteroid (16) Psyche (Hanuš et al. 2013 and Table 2). The power per unit volume, P, of the resulting dynamo is proportional to the Rayleigh number where $P = \gamma Ra_Q$ and

$$\gamma = \frac{3(r_c - r_i c)^2}{2(r_c^3 - r_i c^3) r_c} \left[f_i \left(\frac{3}{5} \frac{r_c^5 - r_i c^5}{r_c^3 - r_i c^3} \right) + 1 - f_i \left(r_c^2 - \frac{3}{5} \frac{r_c^5 - r_i c^5}{r_c^3 - r_i c^3} \right) \right] \tag{16}$$

where f_i is the fraction of inner-boundary originated buoyancy which is taken to be ~ 0.5.

The strength of the magnetic field generated at the core-mantle boundary (B_{cmb}) is given

by:

$$B_{cmb} = c_1 f_{ohm}^{0.5} P^{0.34} (\rho\mu)^{0.5} \Omega D \tag{17}$$

where c_1 is a scaling prefactor (Aubert et al., 2009), ρ is the density of the fluid part of the core, μ is magnetic permeability and f_{ohm} is the fraction of ohmic dissipation. Assuming a planetocentric dipolar field, the strength of the magnetic field at the depth of the pallasites is given by

$$B_{pal} = \left(\frac{r_c}{r_{pal}}\right)^3 B_{cmb} \tag{18}$$

where r_{pal} is the distance from the centre of the parent body to the pallasite depth (constrained by our thermal model).

2.4.2 Maximum magnetic field generation potential

Since dynamo generation in cores undergoing inward solidification is poorly understood and an area of active research, we do not attempt to model dynamo behaviour for this scenario. In order to compare inward versus outward core solidification without invoking a dynamo generation mechanism, we calculated the maximum magnetic field intensity the pallasites could have experienced following the approach of Evans et al. (2018). We consider all energy sources available to the core: gravitational energy (E_G), thermal energy (E_T), latent energy (E_L) and radioactive energy (E_R). Given the small size of the pallasite parent body and the uranium content of the pallasites (85 ppb; Crozaz et al., 1982) we find that radioactive energy is negligible. We also find that thermal and gravitational energy are negligible compared latent energy:

$$E_L = \frac{4}{3}\pi\rho_c \left(r_c^3 - r_{ic}^3\right) L_c \tag{19}$$

The maximum average intensity of the magnetic field (B_{max}) at the depth of the pallasites is given by

$$B_{max} \approx f_{dip} \left(\frac{r_c}{r_{pal}}\right)^3 \sqrt{2\mu c f_{ohm} \bar{\rho_c}^{\frac{1}{3}}} \left(F Q_{cmb}\right)^{\frac{1}{3}} \tag{20}$$

where $Q_{cmb} = \frac{E_L(t)}{A_c \Delta t_c}$ where A_c is the surface area of the core and Δt_c is the length of time over

Symbol	Definition	Value	Units	Reference
δt	Time step	2×10^{11}	s	Bryson et al. (2015)
δr	Incremental radius	1000	m	Bryson et al. (2015)
Δ	Relative slope of solidus vs adiabat	1.2	Nimmo (2009)	
α	Thermal expansivity	9.2×10^{-5}	K^{-1}	Nimmo (2009)
Ω	Rotational frequency	4×10^{-4}	s^{-1}	Hanuš et al. (2013); Bryson et al. (2015)
ρ_c	Core density	7019	kg m^{-3}	Nimmo (2009)
C_p	Specific heat capacity	835	J kg^{-1} K^{-1}	Nimmo (2009)
Φ_v	Ohmic dissipation	0.2 – 2.0	W K^{-1} m^{-3}	Nimmo (2009)
G	Gravitational constant	6.67×10^{-11}	m^3 kg^{-1} s^{-2}	
f_i	Fraction of inner-boundary related buoyancy	0.5		Aubert et al. (2009)
μ	Magnetic permeability	$4\pi \times 10^{-7}$	H m^{-1}	
f_{ohm}	Fraction of ohmic dissipation	1		Aubert et al. (2009)
f_{dip}	Dipolar component	0.14		Evans et al. (2018)
c	constant of proportionality	0.63		Evans et al. (2018)
κ	Mantle diffusivity	5×10^{-7}	$m^2 s^{-1}$	Bryson et al. (2015)
k_m	Mantle thermal conductivity	3	W m^{-1} K^{-1}	Bryson et al. (2015)
k_c	Core thermal conductivity	30	W m^{-1} K^{-1} Nimmo (2009)	
c_1	Scaling prefactor	1.65		Aubert et al. (2009)
F	Efficiency factor	0.05		Evans et al. (2018)

Table 2: A summary of the parameter values used in thermal and dynamo calculations.

which the dynamo is active, f_{dip} is the dipolar fraction of the magnetic field, c is a constant of proportionality and F is an efficiency factor (Evans et al., 2018).

3 Results

3.1 Cloudy Zone Paleointensities

Histograms of XMCD intensity were calculated for the region of cloudy zone adjacent to the tetrataenite rim (Figure 1). The mean XMCD intensity was calculated from the histograms of pixel intensity for eight regions of cloudy zone for each rotation (Table S2). Paleointensities were determined using Equations $1 - 3$ and we found the Springwater cloudy zone records a unidirectional paleointensity of 22 ± 8 μT (Figure 2).

We have also reassessed previous studies on the Imilac, Esquel, Brenham and Marjalahti pallasites and updated their paleointensities and corresponding uncertainties to reflect their analysis in a single rotation (Nichols et al., 2016; Bryson et al., 2015). The original paleointensity estimates were improved upon by Maurel et al. (2019) after the size of the islands in the cloudy zone at the point of remanence acquisition was established. Here we estimate the upper limit on these revised paleointensities to 95% confidence (Table 3).

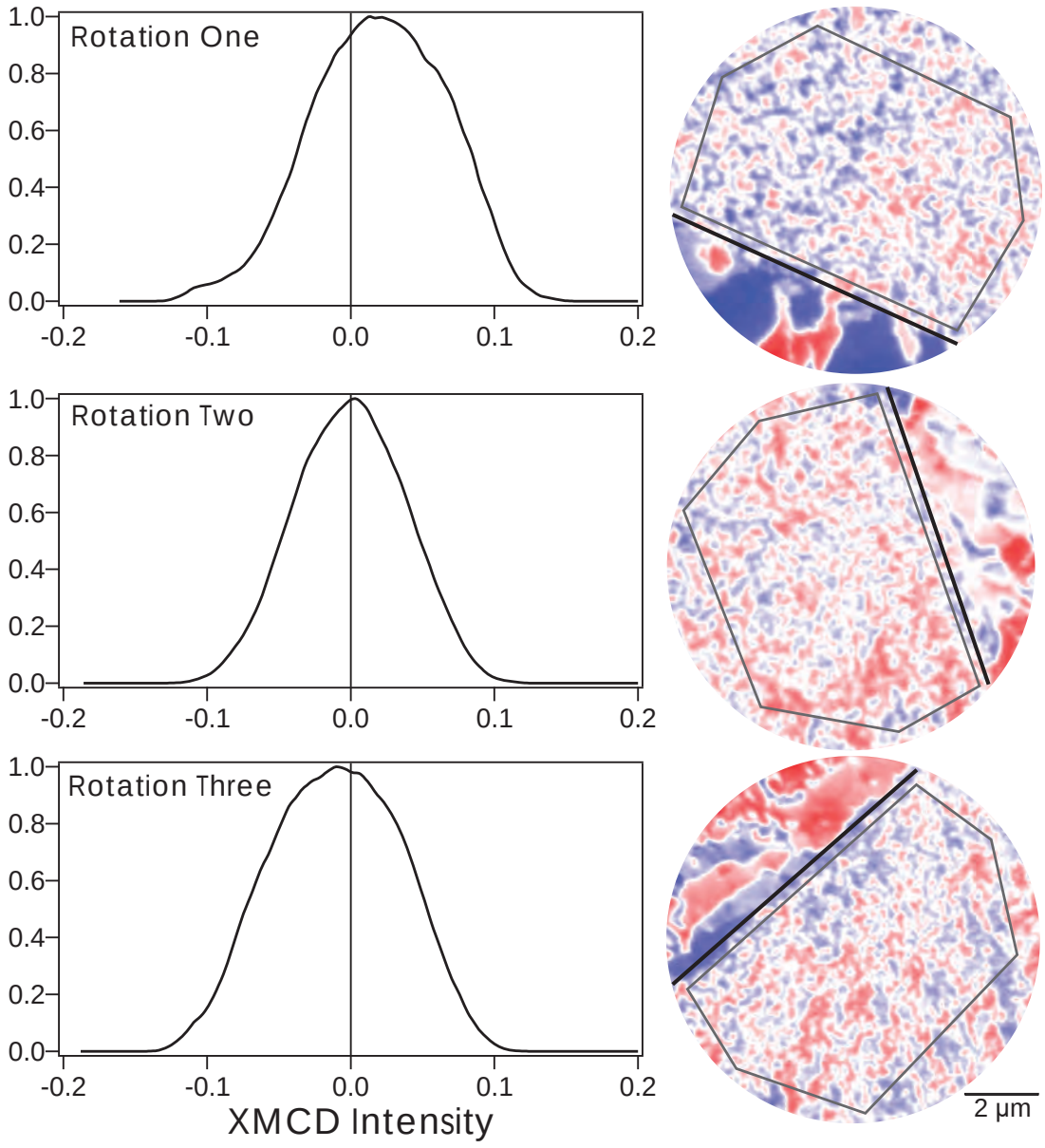

Figure 1: Histograms of pixel intensity for the coarse cloudy zone, and an example of an XMCD image for each rotation. All histograms are corrected using corrections calculated from Equation S1.

Meteorite	**Original paleointensity estimate (μT)**	**Revised paleointensity estimate (μT)**[d]	**Maximum paleointensity estimate* (μT)**[b]
Marjalahti	< 7[a]	0.2	3
Brenham	< 7[a]	0.3	5
Springwater	22 ± 8[b]		
Imilac	119 ± 12[c]	6.8 ± 2.0	80 ± 15
Esquel	84 ± 14[c]	4.8 ± 1.5	64 ± 15

Table 3: A summary of the paleointensity estimates calculated from the cloudy zone for each of the main group pallasites. The first column lists the pallasite measured. The second column lists the original measured paleointensities assuming islands acquire remanence at 30% of their present day diameter (a=Nichols et al. (2016), b=This Study, c=Bryson et al. (2015)). The third column lists the revised paleointensity estimates based on improved understanding of cloudy zone island remanence acquisition at $\sim$ 78% of their present diameter (d=Maurel et al. (2019)). The fourth column lists upper estimates on X-PEEM intensities to 95% confidence by taking into account the uncertainty in measurement direction because they were only imaged in one orientation.

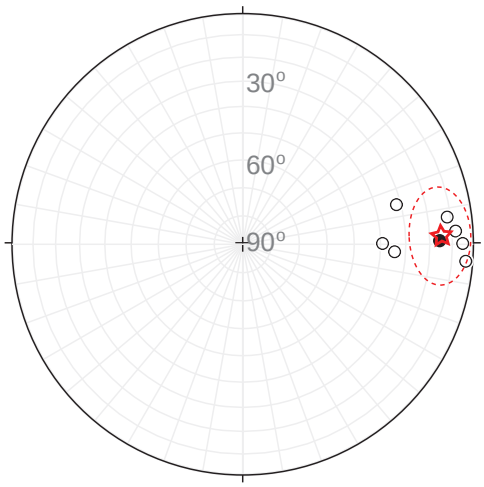

Figure 2: Equal area polar stereonet projection showing the direction of magnetization for the 8 analysed regions of cloudy zone in Springwater imaged using X-PEEM. The results show that magnetization is unidirectional. The mean direction is shown by the red star and the 95% confidence interval on the direction by the dashed red circle. Dashed and open symbols are upper-hemisphere projections, solid symbols are lower-hemisphere projections.

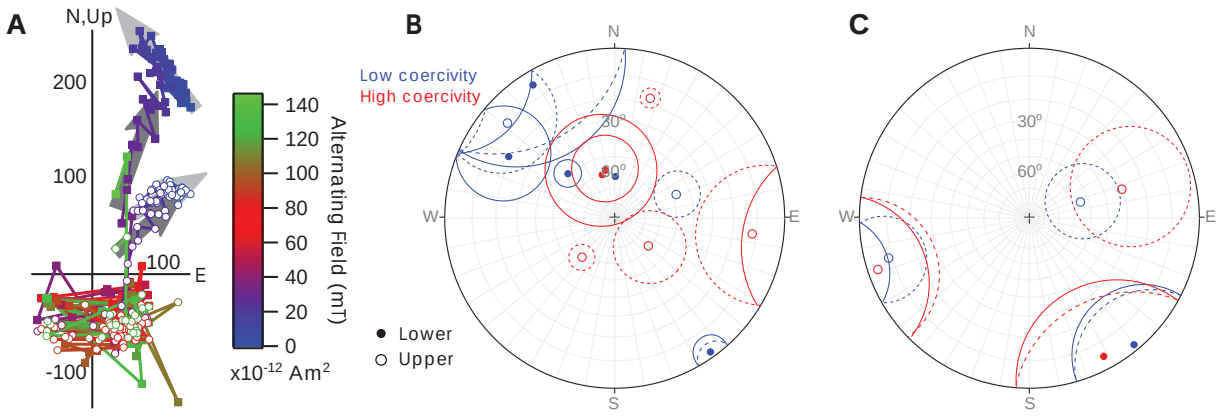

Figure 3: (a) Zijderveld plot for NRM demagnetization of subsample SWH1frag from a Springwater olivine. Closed squares show declination, open circles show inclination, the colour bar represents the strength of AF demagnetization. Low and high coercivity components are shown by the light and dark grey arrows, respectively. (b) Equal area stereographic projection of the NRM directions measured for Springwater (SWH). Blue and red circles denote the low and high coercivity components, respectively. Open circles are points in the upper hemisphere, whilst closed circles are points in the lower hemisphere. The surrounding circles are the α_{95} for each component. (c) Equal area stereographic projection of the NRM directions measured for Imilac (IM).

3.2 Magnetic Behaviour of Olivine Inclusions

3.2.1 Alternating Field Demagnetization

We carried out NRM AF demagnetization of 3 subsamples of Imilac and 11 subsamples of Springwater (Table S6). We found that the 3 subsamples of Springwater taken from the AMNH sample (SW) have been overprinted by a strong IRM (Figure S8) and were therefore discounted from our assessment of the NRMs. For the other subsamples (IM and SWH) low (< 7 mT) and high coercivity ($7 - 35$ mT) components were identified. High coercivity components were forced through the origin. The high coercivity component is poorly defined for many samples, highlighted by high maximum angular deviation (MAD) values ($> 20°$). The directions of the low and high coercivity components were plotted on a stereonet for each set of oriented subsamples from Imilac and Springwater (Figure 3). No evidence was found for a stable direction for low or high coercivity components in either sample, suggesting no primary NRM is recoverable.

We assessed the fidelity of Springwater olivines as remanence carriers by comparing NRM

demagnetization to laboratory applied ARM and IRM demagnetization (Table S5). To quantify the fidelity, we followed the approach of Tikoo et al. (2012) and Bryson et al. (2017). We consider: D', the difference between the applied laboratory field and the retrieved paleointensity; and E, the error associated with the retrieved paleointensity compared to the applied laboratory field, where

$$D' \equiv \frac{I - L}{L} \cdot 100\% \tag{21}$$

and

$$E \equiv \frac{W}{L} \cdot 100\% \tag{22}$$

where L is the laboratory field, I is the retrieved paleointensity and W is the 95 % confidence interval. D' and E were calculated for Springwater using both the ARM method (Equation 5, Figure S9c) and the IRM method (Equation 6, Figure S9d). Results are presented in Table S5. We consider generous acceptance criteria for reliable paleomagnetic recorders; $-50\% > D' < 100\%$ and $E < 100$ % (Bryson et al., 2017). Figure 4 shows results of the fidelity tests, which do not reliably fall within the acceptance criteria suggesting these pallasite olivines are not robust paleomagnetic recorders of magnetic fields < 225 μT, as estimated by ARM and IRM methods.

3.2.2 Controlled-atmosphere thermal demagnetization

We conducted controlled atmosphere IZZI Thellier-Thellier experiments on 5 subsamples of Springwater (SWH) and 6 subsamples of Imilac (Figures S17 and S16). In all cases we found that pTRM checks failed at low temperatures (< 250 °C; Table S8). We found that following heating, nanoscale FeNi particles appeared to have grown along cracks in the olivine crystals (Figure S12). This is consistent with the observed change in the rock magnetic properties of the samples. After heating, the coercivity of the samples had increased (Figure S13) and the hysteresis loops indicate that magnetic carriers with ideal, single-domain characteristics had formed (Figure S15). Quantum diamond microscopy showed that the magnetic phases are

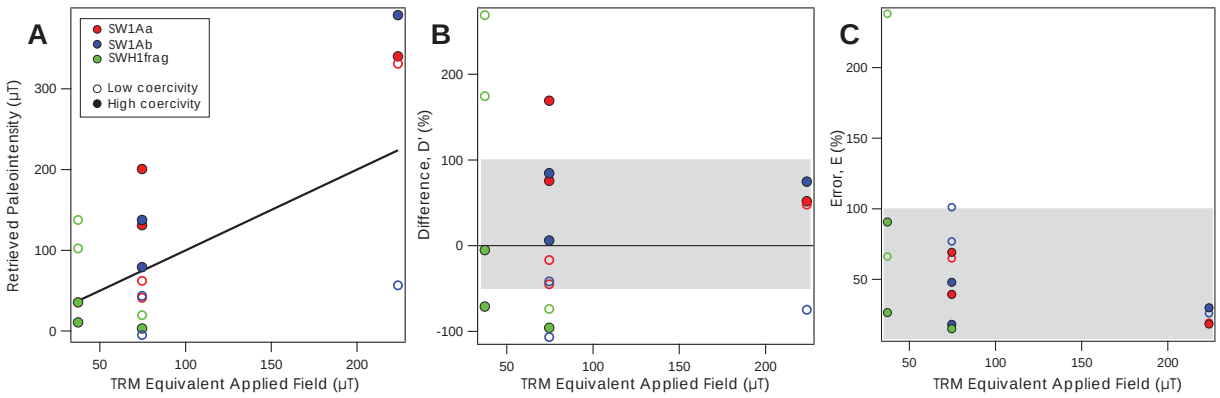

Figure 4: Fidelity tests for SW1Aa, SW1Ab and SWH1frag are shown in red, blue and green, respectively. Paleointensity estimates for low and high coercivity components are shown by open and closed circles, respectively. (a) The retrieved paleointensity versus applied field. The thick black line is a 1:1 relationship between the retrieved paleointensity and applied field. (b) The difference between the retrieved paleointensity and applied field. The grey box shows the region for which paleointensity estimates are acceptable within the arbitrary threshold. (c) The error on the retrieved paleointensity vs applied field. These values should be below the marked 100 % threshold, as shown by the grey box.

concentrated along cracks, however given that these were imaged after applying a saturating IRM of 300 mT we cannot quantify their contribution to the measured NRM (Figure S14).

3.2.3 CO_2 laser thermal demagnetization

IZZI Thellier-Thellier experiments were also conducted on 2 subsamples of Springwater (SWR) in air using a CO_2 laser. An origin-trending component was identified in subsample SWR-TopD3 between 350 – 500 °C, however pTRM checks failed at 305 – 320 °C and therefore demagnetization was not continued to higher temperatures (Figure S18 and Table S9).

3.3 Thermal and dynamo model results for the pallasite parent body

Our experimental data place two important constraints on the cooling model for the pallasite parent body. First, Marjalahti and Brenham acquired a null remanence prior to core solidification. Second, Springwater, Imilac and Esquel acquired paleointensities while a dynamo was active, most likely during core solidification. The model-derived timing of remanence acquisition for each pallasite is given in Table 4.

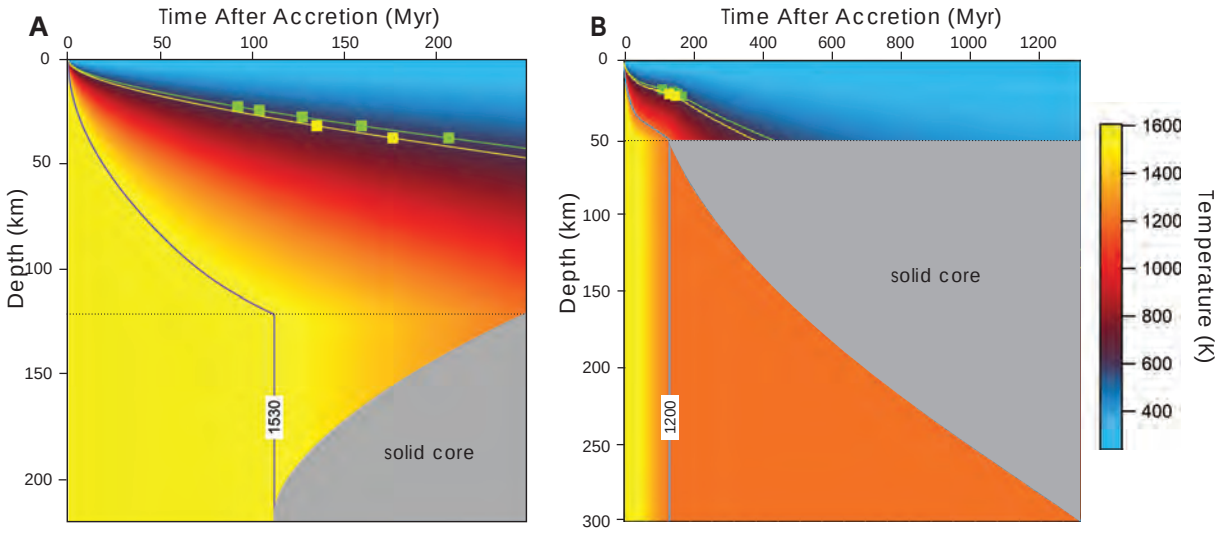

Figure 5: Thermal evolution models for planetesimals with outward and inward core solidification. The green line is the 593 K contour, which is the temperature at which the cloudy zone acquires remanence. The green squares represent the timing of remanence acquisition for the Marjalahti, Brenham, Springwater, Imilac and Esquel cloudy zones. The yellow line is the 633 K contour, which is the temperature at which the pallasite olivines acquire remanence (Tarduno et al., 2012). The yellow squares are for the Imilac and Esquel olivines. The grey region shows the solid part of the core. (a) Thermal model for outward core solidification within a planetesimal of radius 220 km with a core radius of 100 km. The purple line is the 1530 K contour, which is the liquidus of FeS with a composition of 23 wt% S. (b) Thermal model for inward core solidification within a planetesimal of radius 300 km with a core radius of 250 km. The blue line is the 1200 K contour, which is the liquidus of FeS with a composition of 31 wt% S.

Pallasite	Cooling Rate ($^{\circ}$CMyr^{-1})	Inferred depth in parent body (km)	Inferred height above CMB (km)	Time of NRM (Myr after accretion)
Inner core nucleation				
Marjalahti	7.6 ± 0.6	22 ± 1.5	92 ± 20	92 ± 6
Brenham	6.6 ± 0.5	24 ± 1.5	90 ± 20	105 ± 5
Springwater	5.4 ± 0.5	27 ± 2	87 ± 20	129 ± 7
Imilac	4.3 ± 0.3	31 ± 2.5	83 ± 20	163 ± 7
Esquel	3.3 ± 0.6	35 ± 4	79 ± 20	209 ± 8
Outer core nucleation				
Marjalahti	7.6 ± 0.6	21 ± 1	39 ± 5	102 ± 7
Brenham	6.6 ± 0.5	22 ± 1	37 ± 4	119 ± 11
Springwater	5.4 ± 0.5	24 ± 2	36 ± 4	135 ± 6
Imilac	4.3 ± 0.3	26 ± 3	33 ± 3	153 ± 4
Esquel	3.3 ± 0.6	29 ± 5	30 ± 1	176 ± 14

Table 4: Table showing the cooling rates and timing of remanence acquisition for each pallasite studied using paleomagnetism. The first column is the name of the studied pallasite. The second column is the cooling rate of the pallasite (Yang et al., 2010). The third column is the inferred depth of the pallasite within the parent body. The fourth column is the inferred height of the pallasite above the core-mantle boundary. The fifth column is the inferred time of remanence acquisition; the cloudy zone acquires remanence upon cooling through 320 $^{\circ}$C.

For inner core nucleation, we found the thermal evolution of parent bodies with a radius between $180 - 360$ km was consistent with our experimental results (Figure 6a, Table S10). The parent body cannot be have a radius < 180 km because there is insufficient time for Springwater, Imilac and Esquel to acquire remanence before the core is entirely solid. The upper limit on parent body size (360 km) is constrained by the sulfur content of the core; the liquidus temperature must be sufficiently high for core solidification to begin before Springwater acquired its remanence. The FeS liquidus exceeds 1600 K (the silicate solidus) when S < 18 wt% (Ehlers, 1972). Since we assume both the metal and silicate components of the parent body are entirely liquid upon accretion to ensure complete differentiation sulfur contents below 18 wt% are not considered.

For outer core nucleation, all the cooling model solutions for inner core nucleation remain valid, however core solidification extends over significantly longer timescales (Figure 5b). We found that the minimum mantle thickness was also smaller for inward core solidification com-

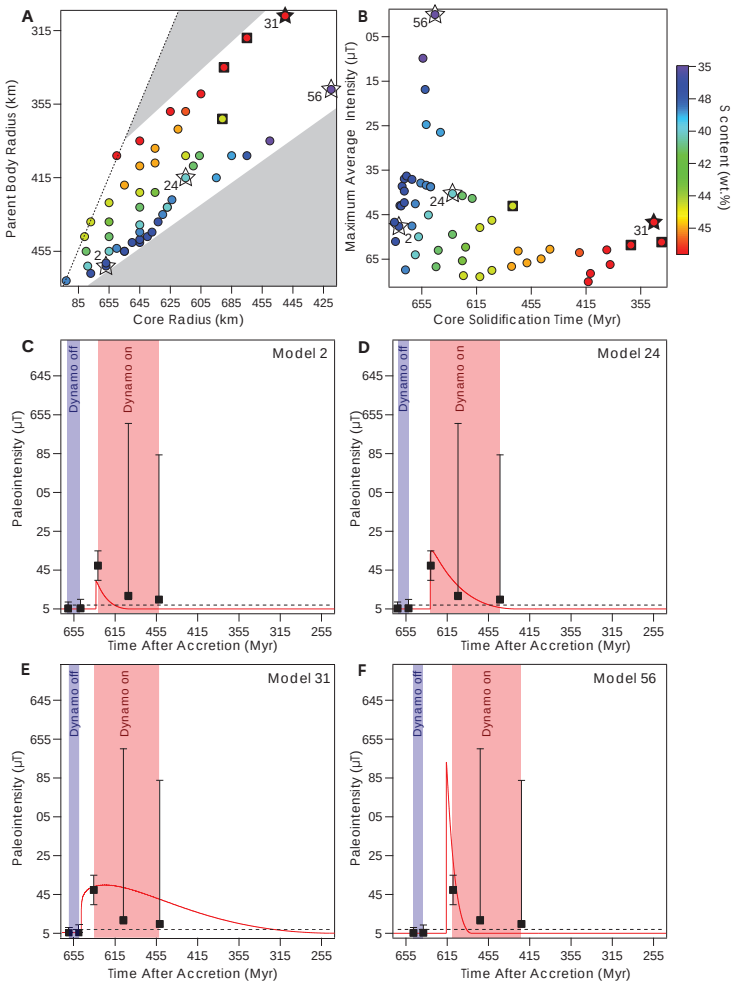

Figure 6: Thermal and dynamo model solutions. (a) The parent body sizes and sulfur compositions that produced cooling models consistent with our experimental data. We only consider core sizes between > 40% of the parent body radius, represented by the black dashed line. Grey regions represent parent body configurations inconsistent with our experimental data. The colour of the points represent their sulfur content. Black squares represent cooling models which also generated a dynamo consistent with our experimental data. Four examples of dynamo model results are highlighted by stars. Closed and open stars are examples of dynamo models shown in that were (e) and were not (c,d,f) consistent with our experimental data. (b) The maximum intensity and core solidification time corresponding to each cooling model shown in (a). (c) Dynamo evolution due to inner core nucleation, for model 2 (Table S10). Black squares and vertical error bars are the measured paleointensities of the pallasite cloudy zones using X-PEEM. The relative timings of remanence acquisition are calculated from the cooling model. The red line shows the evolution of a dynamo driven by core solidifcation. The black dashed line shows the minimum paleointensity that can be attributed to an active dynamo. Model 2 is too weak to explain the measured paleointensities. The shaded regions represent experimental constraints on when there was no dynamo and the core was entirely liquid (blue region) and when there was an active dynamo and the core was solidifying (red region). (d) Model 24 does not sustain a dynamo for long enough to explain the measured paleointensities. (e) Model 31 matches the measured paleointensities. (f) Model 56 generates a dynamo which is too short and intense to explain the measured paleointensities.

pared to outward core solidification for similar sized cores (Figure 7).

For each plausible cooling model solution, we calculated the evolution of a dynamo driven by inner core solidification. The resulting dynamo model was compared to our experimental data (Figure 6). We found that for dynamo evolution to be consistent with our measured paleointensities, relatively long core solidification times ($>$ 180 Myr) and large cores ($>$ 170 km) are required.

Using our planetesimal models for both inward and outward core nucleation, we calculated the maximum intensity that the dynamo could have generated, assuming it was continuously active between the Springwater and Esquel cloudy zones cooling through the tetrataenite ordering temperature. Our results suggest that a planetesimal with a large core and thin mantle has sufficient energy to generate the observed high paleomagnetic field intensities (Figure 7).

4 Discussion

4.1 Pallasites as Paleomagnetic Recorders

In recent years, significant progress has been made to understand how remanence is acquired by the cloudy zone and to improve methods for retrieving a reliable, quantified paleointensity. The first studies on the paleomagnetism of the cloudy zone in pallasites (Bryson et al., 2015; Nichols et al., 2016) assumed that the cloudy zone could record time-resolved information, with the oldest record in the coarsest cloudy zone immediately adjacent to the tetrataenite rim, and the youngest record in the fine cloudy zone, furthest from the tetrataenite rim. Einsle et al. (2018) subsequently showed that the cloudy zone acquires remanence simultaneously upon cooling through 320 °C, when the islands order to tetrataenite. The diameter of the islands at the time of tetrataenite ordering was also found to be much larger (92 – 122 nm; Maurel et al., 2019) than previously assumed (35 – 45 nm; Bryson et al., 2015; Nichols et al., 2016), lowering the paleointensity estimates for Marjalahti, Brenham, Imilac and Esquel (Table 3; Maurel et al., 2019).

The experimental method using X-PEEM to image the distribution of magnetization in the

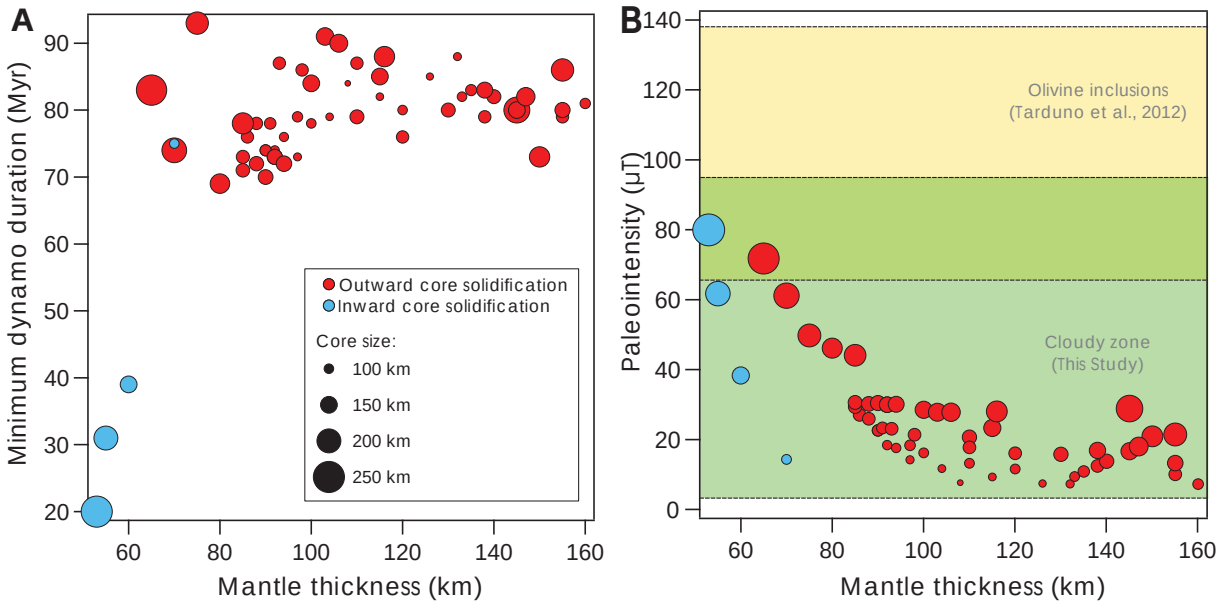

Figure 7: The effect of mantle thickness on dynamo duration and mean dynamo intensity. Red points are for our thermal models for outward core solidification. Blue points are for our thermal models for inward core solidification. The size of the point represents the size of the planetesimal core. (a) Minimum dynamo duration (the time between Springwater and Esquel acquiring remanence) as a function of mantle thickness. For outward solidification, there is little dependence on mantle thickness or core size. For inward core solidification, the dynamo duration depends strongly on mantle thickness. (b) The yellow region represents the paleointensity results reported by Tarduno et al. (2012) for Imilac and Esquel. The green region represents the paleointensities reported here from X-PEEM studies of Springwater, Imilac and Esquel. To generate paleointensities consistent with both sets of observations, the pallasite parent body must have had a large core and thin mantle, regardless of the direction of core solidification.

cloudy zone has also been improved. Previous studies imaged the distribution of magnetization in the cloudy zone in a single orientation (Bryson et al., 2015; Nichols et al., 2016). This does not allow the 3D vector of magnetization to be fully-resolved. Therefore only a minimum paleointensity estimate and minimal (constrained to within a hemisphere) directional information can be recovered. We imaged Springwater in three rotations, adopting the improved method outlined by Bryson et al. (2019a). Therefore the paleointensity and direction (relative to the sample) of magnetization in the Springwater pallasite have been fully resolved. We have also improved upon the paleointensity estimates for Marjalahti, Brenham, Imilac and Esquel calculated by Maurel et al. (2019) by accounting for the fact these paleointensity estimates were only lower limits. We have calculated upper bounds on the true paleointensity and found our results are consistent with the paleointensities reported for Imilac and Esquel olivines (Tarduno et al., 2012).

Given the developments in the understanding of cloudy zone paleomagnetism, we are now able to present the most detailed time-resolved record of paleointensities on the MG pallasite parent body. Further work is still required to understand the role of interactions between cloudy zone islands. However since we have assumed no interaction, accounting for magnetostatic interactions between islands will only increase our paleointensity estimates (Dunlop and Ozdemir, 1997). Despite the significant uncertainty associated with some of the paleointensities, a resolvable increase in paleointensity over time most likely triggered by the onset of dynamo activity, can be resolved and the implications of this record are considered in the following sections.

Single crystal thermal paleointensity methods applied to pallasite olivines are challenging because of the significant time needed in sample selection, preparation and experiments, as well as the potential for thermal alteration. Using techniques previously developed at the University of Rochester (Tarduno et al., 2006) the time for conducting single crystal paleointensity studies typically spans multiple years, rather than the two weeks in which the laser-heated experiments discussed here were conducted at the University of Rochester. Additional experiments using AF and controlled-atmosphere heating techniques were conducted at MIT over three months. Our AF experiments demonstrated the poor recording fidelity of pallasite olivines, which cannot

reliably record paleointensities < 225 μT using ARM and IRM methods. Controlled-atmosphere experiments were also unable to prevent olivine alteration. In contrast, some olivines can be cycled through multiple TRMs and show properties meeting Thellier's criteria (Tarduno et al., 2012). Springwater olivines are 18% fayalitic (Righter et al., 1990) and Imilac olivines are 12.3% fayalitic (Wasson and Choi, 2003) suggesting they have an equivalent oxygen fugacity at high temperatures (Righter et al., 1990). However, experimental evidence suggests pallasite fugacity can vary significantly (Brett and Sato, 1984; Holmes and Arculus, 1982). Given the rapid alteration of olivines at low temperatures (150 °C) it appears our samples were not in equilibrium with the controlled atmosphere. The growth of nanoscale FeNi particles may be indicative that the atmosphere (IW-2) was too reducing.

Previous studies (Tarduno et al., 2012; Tarduno and Cottrell, 2013) reported successful thermal demagnetization of olivines from the Imilac, Esquel and Springwater pallasites. The method used for these studies involved heating samples with a CO_2 laser in air with short heating and cooling times of a few minutes. The null success rate for our controlled-atmosphere thermal experiments is possibly attributed to the low number of samples measured [7 for Springwater (SWH) and 6 for Imilac] are similar to the unsuccessful results reported by Tarduno et al. (2012) and further indicate that only some millimeter-sized pallasite olivines have inclusions that can be retrieved by heating. We suggest that at least twice as many specimens should be measured as studied here to obtain paleointensity values. This is supported by our identification of a stable remanence component in only one of our Springwater specimens, SWRTopD3 (Figure S18), which suggests preservation of magnetic minerals recording a primary magnetization. The experimental challenges encountered when measuring pallasite olivines highlights the benefits of studying the cloudy zone. Our X-PEEM technique does not require sample heating and therefore offers an effective approach for recovering paleointensities without risk of sample alteration. However, the availability of results from pallasite olivines is important in our following discussion because results obeying Thellier Laws are independent of those acquired using X-PEEM and the fact that both yield results indicating a past magnetization gives us confidence in our further consideration of the interior dynamics and structure of the pallasite

parent body.

4.2 Time resolved records of magnetic activity on the Main Group pallasite parent body

We present a comprehensive time-resolved paleomagnetic record for the MG pallasite parent body. We have used these paleomagnetic observations to constrain the thermal evolution of the pallasite parent body following a similar approach to Tarduno et al. (2012) and Bryson et al. (2015). Assuming that the dynamo was driven by core solidification, Brenham and Marjalahti acquired a null remanence (or experienced magnetic field intensities too weak to attribute to an active dynamo) prior to the onset of solidification, while Springwater, Imilac and Esquel acquired remanence while the core was still partially liquid consistent with predictions for asteroid dynamo behaviour (Bryson et al., 2019a). Previous studies only considered eutectic solidification of FeS at 1200 K, corresponding to a sulfur content of 31 wt.% (Tarduno et al., 2012; Bryson et al., 2015, 2019a). For solidification at the eutectic, we found that for parent bodies which were sufficiently small for Springwater to acquire remanence after the onset of core solidification, Esquel could not have acquired remanence before core solidifcation was complete. It should also be noted that eutectic solidification of the core will in fact not drive a thermochemical dynamo, although it is a reasonable approximation for considering the thermal evolution of a core. We therefore consider lower sulfur compositions in our planetary cooling model which correspond to higher FeS liquidus temperatures. The raised liquidus temperature causes core solidification to begin at earlier times, and allows a thicker mantle, resulting in slower cooling and longer solidification times. By varying the sulfur content and core size, we found a range of plausible parent body sizes from $180 - 360$ km radius, a larger upper limit than that reported by Bryson et al. (2015). We found that permittable parent body sizes increase with decreasing sulfur content and increasing core size (Figure 6).

4.3 Implications for core crystallisation and dynamo generation

We have considered both outward and inward core solidification for the pallasite parent body. In both cases we assume concentric growth and do not account for the possibility of dendritic growth or other more exotic styles of crystallization (Scheinberg et al., 2016). Our models can therefore be considered as lower limits on the time of core solidification. This does not effect the implications of our results, which primarily depend upon the core beginning to solidify between the times at which Brenham and Springwater acquired remanences, and being sufficiently molten to drive an active dynamo when Esquel acquired its remanence. We found that both inward and outward core growth are consistent with our X-PEEM results, and therefore both solidification styles are considered in the context of dynamo generation.

We present a simple model of dynamo generation via inner core nucleation where the onset of core solidification is accompanied by a rapid increase in magnetic field intensity (Figure 6). There is a gradual decrease in dynamo strength as the liquid, convecting outer shell reduces in volume throughout solidification. This mechanism of core solidification can sustain a long-lived dynamo, supported by current observations of Earth's magnetic field, and modelling of long-lived lunar dynamo activity (Laneuville et al., 2014). If the dynamo was only active for some fraction of the total core solidification time, then the maximum possible magnetic field intensities will be higher; however our measured paleointensity for the Springwater pallasite (22 ± 8 μT), which corresponds to the maximum field strength shortly after the onset of a compositional dynamo, suggests the mean intensity must be relatively weak (< 20 μT). This is consistent with the long lifetime of the dynamo ($> 117 \pm 4$ Myr), which corresponds to the time between Springwater and Esquel acquiring remanence.

We found that a dynamo driven by inner core nucleation is difficult to reconcile with our upper paleointensity limits for Imilac and Esquel and the results reported by Tarduno et al. (2012). As the inner core crystallizes, the dynamo loses power, at odds with the apparent increase in paleointensity recorded by Springwater, Imilac and Esquel, respectively. This discrepancy cannot be explained by the greater depth of each pallasite within the parent body (Table 4) which only accounts for a small increase in intensity. Additionally, the total energy

in the core is insufficient to explain the paleointensities recorded by Imilac and Esquel at their modelled depths within the parent body, even for the shortest possible dynamo duration (Figure 7).

Given the small planetesimal sizes derived from our cooling models, the core is at low pressure, which suggests core solidification is in fact more likely to be initiated at the core-mantle boundary (Hauck et al., 2006; Williams, 2009). We therefore also consider inward core solidification, but do not attempt to model the corresponding dynamo evolution since this is a relatively unexplored phenomena, particularly for a mantled planetesimal. However, model results have demonstrated that inward core solidification can drive a dynamo (Neufeld et al., 2019; Scheinberg et al., 2016) and that some asteroid cores solidified in such a manner (Yang et al., 2007). We find that both inward and outward core solidification of a planetesimal with a large core and thin mantle can explain both the timings of pallasite remanence acquisition relative to core solidification, and the high paleointensities and dynamo lifetime required by our recovered paleomagnetic record (Figure 7). We therefore conclude that a large core ($>$ 200 km radius) and small mantle thickness ($<$ 70 km) are more important for generating high paleointensities than inward vs outward core solidification.

4.4 Implications for the origin of pallasites

A recent study suggested that pallasite formation may be the result of the propagation of metallic dykes from the core-mantle boundary into a shallow overlying mantle (Johnson et al., 2019). This study predicts that for high sulfur compositions ($\sim$ 31 wt%), metallic dykes could penetrate tens of kilometres into the mantle. This is consistent with our model results for inward core solidification (Table 4) which suggest the pallasite parent body had a large metallic core with a high sulfur content and the pallasites could have originated from short distances ($\sim$ 30 km) above the core-mantle boundary. This also demonstrates that the pallasites could form close to the core-mantle boundary while still originating in the mid-mantle of their parent planetesimal as suggested by previous studies (Tarduno et al., 2012; Bryson et al., 2015; Yang et al., 2010).

Pallasites have also been suggested to form throughout the parent body mantle, with the metal representing residual melt left over from incomplete differentiation (Boesenberg et al., 2012; Mckibbin et al., 2019). Textural and geochemical evidence suggests that in addition to residual metallic melt in the mantle, differentiated metal from an impactor must also play a role in pallasite formation in order to explain the range of observed textures (Tarduno et al., 2012; Walte et al., 2020). To reconcile these parent body configurations, where slow-cooled pallasites form close to the core-mantle boundary but also acquire a paleomagnetic record of a convecting, liquid core requires inward core solidification (Mckibbin et al., 2019), consistent with our results. We also note however, that if the pallasite parent body only underwent partial differentiation, the metallic core will be relatively small, at odds with the energy required to drive a sustained, high-intensity dynamo (Figure 7). This may suggest the parent body must be relatively large (radius $>$ 300 km) in order to partially differentiate and still form a core large enough to explain the observed paleointensities.

It has also been hypothesized that the pallasites may form within a planetesimal similar to the metallic asteroid (16) Psyche (Elkins-Tanton et al., 2020; Johnson et al., 2019; Walte et al., 2020). Current estimates suggest Psyche has a density of 4160 $\pm$ 640 kgm^{-3} (Drummond et al., 2018). This is comparable to the density for many of our planetesimal models, assuming the core has a density of 7000 kgm^{-3} and the mantle has a density of 3000 kgm^{-3} (Figure 8). For our cooling models where intensities are consistent with our X-PEEM observations the model planetesimals have a similar density to Psyche. To explain both our X-PEEM observations and the paleointensities recovered from olivine inclusions (Tarduno et al., 2012) requires a large-cored and thinly-mantled planetesimal with a density slightly higher than current predictions for Psyche.

5 Conclusions

We have presented new paleomagnetic data for the Springwater pallasite which 'fills the gap' between Brenham and Marjalahti acquiring remanence prior to core solidification (Nichols et al.,

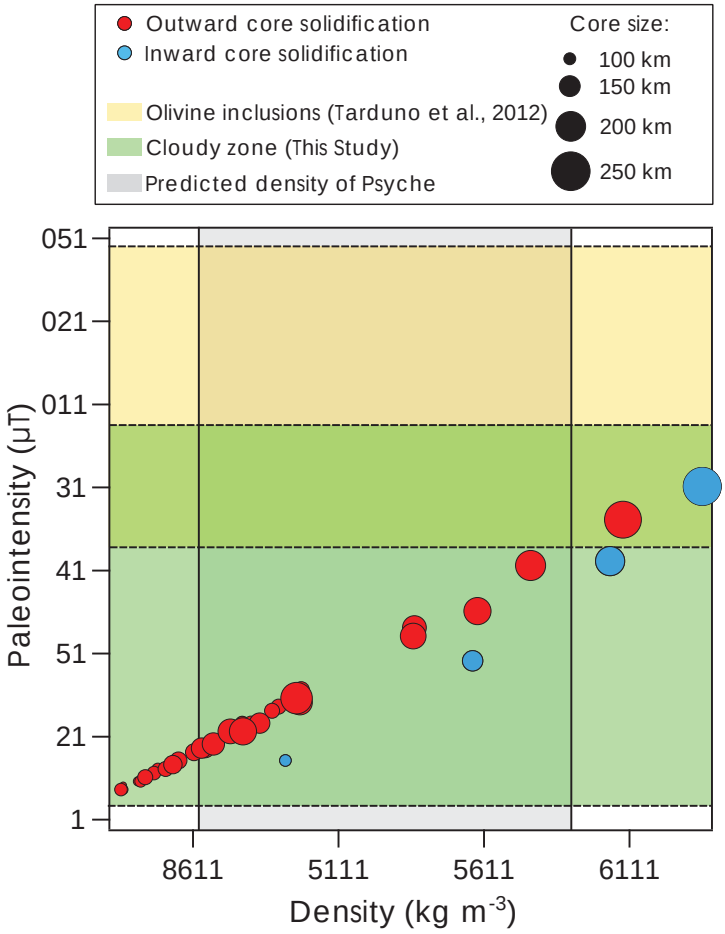

Figure 8: The magnetic field intensity vs planetesimal density predicted for each of our cooling models assuming an average density of 7000 kgm^{-3} for the core and 3000 kgm^{-3} for the mantle. Red points are for our thermal models for outward core solidification. Blue points are for our thermal models for inward core solidification. The size of the point represents the size of the planetesimal core. The yellow region represents the paleointensity results reported by Tarduno et al. (2012) for Imilac and Esquel. The green region represents the paleointensities reported here from X-PEEM studies of Springwater, Imilac and Esquel. The grey region represent the predicted density of asteroid (16) Psyche (Drummond et al., 2018).

2016) and Imilac and Esquel acquiring remanence after core solidification had begun and a compositional dynamo was active (Tarduno et al., 2012; Bryson et al., 2015). We have reassessed all X-PEEM data for the pallasites in light of advances in the technique and our understanding of remanence acquisition in the cloudy zone (Einsle et al., 2018; Bryson et al., 2019a; Maurel et al., 2019). In addition, we conducted thermal and AF demagnetization experiments on olivines from the Springwater and Imilac pallasites. We found that AF techniques were not well suited for isolating directions or intensities in the samples analysed. The extensive time (years) required to extract paleointensities from pallasite olivines, and issues with thermal alteration during controlled-atmosphere experiments, highlight the benefit of conducting paleomagnetic analyses on the cloudy zone rather than silicate inclusions in extraterrestrial samples with variable oxygen fugacities. However, previous paleointensity estimates from pallasite olivines (Tarduno et al., 2012) are critical for corroborating our cloudy zone paleointensities; the fact that both yield similar results indicating a past magnetization gives us confidence in our further consideration of the interior dynamics and structure of the pallasite parent body.

We present the most complete time-resolved paleomagnetic record for a planetesimal to date. Our results constrain the onset of core solidification and give a minimum time for core solidification, allowing the size and thermal evolution of the MG pallasite parent body to be well determined. We found that our X-PEEM results are consistent with both inward and outward core solidification, and the temporal trend in paleointensities is consistent with a dynamo driven by inner core solidification. However, to explain the upper limit on our paleointensity determinations for Imilac and Esquel and the strong paleointensities recovered by Tarduno et al. (2012), we show that a planetesimal with a large core and thin mantle is required. Strong paleointensities ($\sim 65 - 95$ μT) in the middle of a thin mantle can be generated by either inward or outward core crystallization. A dynamo driven by inward crystallization has been proposed for the asteroid (16) Psyche (Scheinberg et al., 2016; Neufeld et al., 2019). We show that the pallasites could form relatively close to the core-mantle boundary, while still forming in the middle of a thin mantle as predicted by previous studies (Tarduno et al., 2012; Bryson et al., 2015; Yang et al., 2010). We conclude that the pallasites could form on a planetesimal

like asteroid (16) Psyche, and could form by the intrusion of sulfur-rich metallic dykes through the mantle from the underlying core (Johnson et al., 2019).

Future studies should focus on directly determining the thermochronology of the pallasites. Our thermal models for outward versus inward core solidification provide contrasting predictions for the timing of remanence acquisition and the size of the parent body (Figure 7). Combined thermochronologic and paleomagnetic studies on suites of meteorites from the same parent body can provide a wealth of information regarding the size, internal structure and dynamics of planetesimals.

Acknowledgements

This work was supported by the European Research Council under the European Union's Seventh Framework Programme (FP/2007-2013)/ ERC grant agreement numbers 320750 and 312284. We acknowledge the Helmholtz-Zentrum Berlin for the use of the synchrotron radiation beam time at beamline UE49 of BESSY II. We thank the Natural History Museum, London, the American Museum of Natural History and the Harvard Museum of Natural History for loan of samples. CION thanks the Simons Foundation (Award #556352), The Geological Society, the Mineralogical Society of Great Britain, the Mineral Physics Group of Great Britain, Jesus College Cambridge and the Royal Astronomical Society for funding. BPW thanks the NASA Solar System Workings program and T.F. Peterson, Jr. for support. JHA thanks the Spanish MCINN Project (DWARFS MAT2017-83468-R). Work at the University of Rochester was supported by NSF grant EAR1656348 and NASA grant 80NSSC19K0510. All data associated with this study are available on zenodo (https://doi.org/10.5281/zenodo.4672000).

References

Julien Aubert, Stéphane Labrosse, and Charles Poitou. Modelling the palaeo-evolution of the geodynamo. *Geophysical Journal International*, 179(3):1414–1428, 2009. ISSN 0956540X. doi: 10.1111/j.1365-246X.2009.04361.x.

Joseph S. Boesenberg, Jeremy S. Delaney, and Roger H. Hewins. A petrological and chemical reexamination of Main Group pallasite formation. *Geochimica et Cosmochimica Acta*, 89:134–158, 2012. ISSN 00167037. doi: 10.1016/j.gca.2012.04.037. URL http://dx.doi.org/10.1016/j.gca.2012.04.037.

Robin Brett and Motoaki Sato. Intrinsic oxygen fugacity measurements on seven chondrites, a pallasite, and a tektite and the redox state of meteorite parent bodies. *Geochimica et Cosmochimica Acta*, 48:111–120, 1984.

J. F.J. Bryson, B. P. Weiss, B. Getzin, J. N.H. Abrahams, F. Nimmo, and A. Scholl. Paleomagnetic Evidence for a Partially Differentiated Ordinary Chondrite Parent Asteroid. *Journal of Geophysical Research: Planets*, 124(7):1880–1898, 2019a. ISSN 21699100. doi: 10.1029/2019JE005951.

James F J Bryson, Claire I O Nichols, Julia Herrero-Albillos, Florian Kronast, Takeshi Kasama, Hossein Alimadadi, Gerrit van der Laan, Francis Nimmo, and Richard J Harrison. Long-lived magnetism from solidification-driven convection on the pallasite parent body. *Nature*, 517 (7535):472–475, 2015. ISSN 0028-0836. doi: 10.1038/nature14114.

James F.J. Bryson, Nathan S. Church, Takeshi Kasama, and Richard J. Harrison. Nanomagnetic intergrowths in FeNi meteoritic metal. The potential for time resolved records of planetesimal dynamo fields. *Earth and Planetary Science Letters*, 388:237–248, feb 2014. ISSN 0012821X. doi: 10.1016/j.epsl.2013.12.004. URL http://linkinghub.elsevier.com/retrieve/pii/S0012821X13007012.

James F.J. Bryson, Benjamin P. Weiss, Richard J. Harrison, Julia Herrero-Albillos, and Florian Kronast. Paleomagnetic evidence for dynamo activity driven by inward crystallisation of a metallic asteroid. *Earth and Planetary Science Letters*, 472:152–163, 2017. ISSN 0012821X. doi: 10.1016/j.epsl.2017.05.026.

James F.J. Bryson, Jerome A. Neufeld, and Francis Nimmo. Constraints on asteroid magnetic field evolution and the radii of meteorite parent bodies from thermal modelling. *Earth and Planetary Science Letters*, 521:68–78, 2019b. ISSN 0012821X. doi: 10.1016/j.epsl.2019.05.046. URL https://doi.org/10.1016/j.epsl.2019.05.046.

U. R. Christensen and J. Aubert. Scaling properties of convection-driven dynamos in rotating spherical shells and application to planetary magnetic fields. *Geophysical Journal International*, 166(1):97–114, 2006. ISSN 0956540X. doi: 10.1111/j.1365-246X.2006.03009.x.

Robert S Coe, S. Grommé, and E.A. Mankinen. Geomagnetic paleointensities from radiocarbon-dated lava flows on Hawaii and the question of the Pacific nondipole low. *Journal of Geophysical Research*, 83(B4):1740–1756, 1978. ISSN 0148-0227. doi: 10.1029/JB083iB04p01740.

Ghislaine Crozaz, Scott F. Sibley, and Douglas R. Tasker. Uranium in the silicate inclusions of stony-iron and iron meteorites. *Geochimica et Cosmochimica Acta*, 46(5):749–754, 1982. ISSN 00167037. doi: 10.1016/0016-7037(82)90026-6.

K Dodds, James F.J. Bryson, Jerome A. Neufeld, and Richard J. Harrison. The early thermal evolution of planetesimals during accretion and differentiation and its consequences for dynamo generation by thermally-driven convection. *Journal of Geophysical Research: Planets*, 2021.

Jack D. Drummond, William J. Merline, Benoit Carry, Al Conrad, Vishnu Reddy, Peter Tamblyn, Clark R. Chapman, Brian L. Enke, Imke de Pater, Katherine de Kleer, Julian Christou, and Christophe Dumas. The triaxial ellipsoid size, density, and rotational pole of asteroid (16) Psyche from Keck and Gemini AO observations 2004–2015. *Icarus*, 305:174–185, 2018. ISSN 10902643. doi: 10.1016/j.icarus.2018.01.010. URL `https://doi.org/10.1016/j.icarus.2018.01.010`.

David J. Dunlop and Ozden Ozdemir. *Rock Magnetism Fundamentals and Frontiers*. Cambridge University Press, 1997.

Ernest G Ehlers. *Interpretation of geological phase diagrams*. WH Freeman, 1972.

Joshua F. Einsle, Alexander S. Eggeman, Benjamin H. Martineau, Zineb Saghi, Sean M. Collins, Roberts Blukis, Paul A. J. Bagot, Paul A. Midgley, and Richard J. Harrison. Nanopaleomagnetic properties of the meteorite cloudy zone. *Proceedings of the National Academy of Sciences*, XXX(Xx), 2018. ISSN 0027-8424. doi: 10.1073/pnas.XXXXXXXXXX. URL `http://arxiv.org/abs/1803.11502`.

Linda T. Elkins-Tanton, Benjamin P. Weiss, and Maria T. Zuber. Chondrites as samples of differentiated planetesimals. *Earth and Planetary Science Letters*, 305:1–10, may 2011. ISSN 0012821X. doi: 10.1016/j.epsl.2011.03.010. URL `http://linkinghub.elsevier.com/retrieve/pii/S0012821X11001543`.

L.T. Elkins-Tanton, E. Asphaug, J.F. Bell, H. Bercovici, B. Bills, R. Binzel, W.F. Bottke, S. Dibb, D.J. Lawrence, S. Marchi, T.J. McCoy, R. Oran, R.S. Park, P.N. Peplowski, C.A. Polanskey, T.H. Prettyman, C.T. Russell, L. Schaefer, B.P. Weiss, M.A. Wieczorek, D.A. Williams, and M.T. Zuber. *Observations, meteorites, and models: A pre-flight assessment of the composition and formation of (16) Psyche*. 2020. ISBN 0000000218047. doi: 10.1029/2019JE006296. URL `https://onlinelibrary.wiley.com/doi/abs/10.1029/2019JE006296`.

Alexander J Evans, Sonia M Tikoo, and Jeffrey C Andrews-Hanna. The case against an early lunar dynamo powered by core convection. *Geophysical Research Letters*, pages 98–107, 2018. doi: 10.1002/2017GL075441.

Roger R. Fu, Eduardo A. Lima, Michael W.R. Volk, and Raisa Trubko. High-Sensitivity Moment Magnetometry With the Quantum Diamond Microscope. *Geochemistry, Geophysics, Geosystems*, 21(8):1–17, 2020. ISSN 15252027. doi: 10.1029/2020GC009147.

M Fuller and S. M. Cisowski. Lunar Paleomagnetism. 1987.

Ian Garrick-Bethell, Benjamin P Weiss, David L Shuster, and Jennifer Buz. Early lunar magnetism. *Science*, 323(5912):356–9, jan 2009. ISSN 1095-9203. doi: 10.1126/science.1166804.

J. Gattacceca and P. Rochette. Toward a robust normalized magnetic paleointensity method applied to meteorites. *Earth and Planetary Science Letters*, 227(3-4):377–393, 2004. ISSN 0012821X. doi: 10.1016/j.epsl.2004.09.013.

D R Glenn, R R Fu, P Kehayias, D Le Sage, E A Lima, B P Weiss, and R L Walsworth. Micrometer-scale magnetic imaging of geological samples using quantum diamond microscopy. *Geochem. Geophys. Geosyst.*, (4 mm), 2017. ISSN 15252027. doi: 10.1002/2017gc006946. URL `https://arxiv.org/ftp/arxiv/papers/1707/1707.06714.pdf`.

R. C. Greenwood, I. A. Franchi, A. Jambon, J. A. Barrat, and T. H. Burbine. Oxygen usotope variation in stony-iron meteorites. *Science*, 313(5794):1763–1765, 2006. ISSN 10959203. doi: 10.1126/science.1128865.

J. Hanuš, F. Marchis, and J. Ďurech. Sizes of main-belt asteroids by combining shape models and Keck adaptive optics observations. *Icarus*, 226(1):1045–1057, 2013. ISSN 00191035. doi: 10.1016/j.icarus.2013.07.023.

Steven A. Hauck, Jonathan M. Aurnou, and Andrew J. Dombard. Sulfur's impact on core evolution and magnetic field generation on Ganymede. *Journal of Geophysical Research*, 111(E09008):1–14, 2006. ISSN 0148-0227. doi: 10.1029/2005JE002557. URL `http://doi.wiley.com/10.1029/2005JE002557`.

R. D. Holmes and Richard J. Arculus. Metal-Silicate Redox Reactions: Implications for core-mantle equilibrium and the oxidation state of the upper mantle. *Abstracts of Papers presented to the conference on Planetary Volatiles, held in Alexandria, Minnesota, October 9-12, 1982*, 53(9):1689–1699, 1982. ISSN 1098-6596. doi: 10.1017/CBO9781107415324.004.

Brandon C. Johnson, Michael M. Sori, and Alexander J. Evans. Ferrovolcanism on metal worlds and the origin of pallasites. *Nature Astronomy*, pages 1–4, 2019. ISSN 2397-3366. doi: 10.1038/s41550-019-0885-x.

F. Kronast, J. Schlichting, F. Radu, S. K. Mishra, T. Noll, and H. A. Dürr. Spin-resolved photoemission microscopy and magnetic imaging in applied magnetic fields. *Surface and Interface Analysis*, 42(10-11):1532–1536, 2010. ISSN 01422421. doi: 10.1002/sia.3561.

M. Laneuville, M. A. Wieczorek, D. Breuer, J. Aubert, G. Morard, and T. Rückriemen. A long-lived lunar dynamo powered by core crystallization. *Earth and Planetary Science Letters*, 401:251–260, 2014. ISSN 0012821X. doi: 10.1016/j.epsl.2014.05.057.

Clara Maurel, Benjamin P. Weiss, and James F.J. Bryson. Meteorite cloudy zone formation as a quantitative indicator of paleomagnetic field intensities and cooling rates on planetesimals. *Earth and Planetary Science Letters*, 513:166–175, 2019. ISSN 0012821X. doi: 10.1016/j.epsl.2019.02.027. URL `https://doi.org/10.1016/j.epsl.2019.02.027`.

Seann J Mckibbin, Lidia Pittarello, Christina Makarona, Christopher Hamann, Lutz Hecht, Stepan M Chernonozhkin, Steven Goderis, and Philippe Claeys. Petrogenesis of main group

pallasite meteorites based on relationships among texture, mineralogy, and geochemistry. 31, 2019. doi: 10.1111/maps.13392.

A. R. Muxworthy and W. Williams. Critical single-domain grain sizes in elongated iron particles: implications for meteoritic and lunar magnetism. *Geophysical Journal International*, 202(1):578–583, 2015. ISSN 0956-540X. doi: 10.1093/gji/ggv180. URL http://gji.oxfordjournals.org/cgi/doi/10.1093/gji/ggv180.

Jerome A. Neufeld, James F.J. Bryson, and Francis Nimmo. The Top-Down Solidification of Iron Asteroids Driving Dynamo Evolution. *Journal of Geophysical Research: Planets*, 124 (5):1331–1356, 2019. ISSN 21699100. doi: 10.1029/2018JE005900.

Claire I O Nichols, James F.J. Bryson, Julia Herrero-Albillos, Florian Kronast, Francis Nimmo, and Richard J. Harrison. Pallasite Paleomagnetism: Quiescence of a Core Dynamo. *Earth and Planetary Science Letters*, 441:103–112, 2016.

F. Nimmo. Energetics of asteroid dynamos and the role of compositional convection. *Geophysical Research Letters*, 36(L10201):1–6, may 2009. ISSN 0094-8276. doi: 10.1029/2009GL037997. URL http://doi.wiley.com/10.1029/2009GL037997.

Timothy O'Brien, John A Tarduno, Atma Anand, Jonathan Carroll-nellenback, Alexander N Krot, Aleksey V Smirnov, and Eric G Blackman. Arrival and magnetization of carbonaceous chondrites in the asteroid belt before 4562 million years ago. *Communications Earth & Environment*, pages 1–7, 2020. ISSN 2662-4435. doi: 10.1038/s43247-020-00055-w. URL http://dx.doi.org/10.1038/s43247-020-00055-w.

Kevin Righter, Richard J. Arculus, John W. Delano, and Cassi Paslick. Electrochemical measurements and thermodynamic calculations of redox equilibria in pallasite meteorites: Implications for the eucrite parent body. *Geochimica et Cosmochimica Acta*, 54(6):1803–1815, 1990. ISSN 00167037. doi: 10.1016/0016-7037(90)90409-E.

A. Scheinberg, L. T. Elkins-Tanton, G. Schubert, and D. Bercovici. Core solidification and dynamo evolution in a mantle-stripped planetesimal. *Journal of Geophysical Research E: Planets*, 121(1):2–20, 2016. ISSN 21699100. doi: 10.1002/2015JE004843.

A. Stephenson and D. W. Collinson. Lunar magnetic field palaeointensities determined by an anhysteretic remanent magnetization method. *Earth and Planetary Science Letters*, 23: 220–228, 1974. ISSN 0012821X. doi: 10.1016/0012-821X(74)90196-4.

Clement Suavet, Benjamin P Weiss, and Timothy L Grove. Controlled-atmosphere thermal demagnetization and paleointensity analyses of extraterrestrial rocks. *Geochemistry, Geophysics, Geosystems*, 15:2733–2743, 2014. doi: 10.1002/2013GC005215.Received.

J A Tarduno and Rory D Cottrell. Paleomagnetism of the Springwater Pallasite: Further evidence for a dynamo in the Main Group Pallasite Parent Body. *44th Lunar and Planetary Science Conference*, (2801), 2013.

J A Tarduno, R D Cottrell, and A V Smirnov. The Paleomagnetism of Single Silicate Crystals : Recording Geomagnetic Field Strength During Mixed Polarity Intervals, Superchrons, and Inner Core Growth. (2005):1–31, 2006. doi: 10.1029/2005RG000189.1.Department.

John a Tarduno, Rory D Cottrell, Francis Nimmo, Julianna Hopkins, Julia Voronov, Austen Erickson, Eric Blackman, Edward R D Scott, and Robert McKinley. Evidence for a dynamo in the main group pallasite parent body. *Science*, 338(6109):939–942, nov 2012. ISSN 1095-9203. doi: 10.1126/science.1223932. URL http://www.ncbi.nlm.nih.gov/pubmed/23161997.

Lisa Tauxe and Hubert Staudigel. Strength of the geomagnetic field in the cretaceous normal superchron: New data from submarine basaltic glass of the troodos ophiolite. *Geochemistry, Geophysics, Geosystems*, 5(2):1–16, 2004. ISSN 15252027. doi: 10.1029/2003GC000635.

Sonia M. Tikoo, Benjamin P. Weiss, Jennifer Buz, Eduardo A. Lima, Erin K. Shea, Gabriela Melo, and Timothy L. Grove. Magnetic fidelity of lunar samples and implications for an ancient core dynamo. *Earth and Planetary Science Letters*, 337-338:93–103, 2012. ISSN 0012821X. doi: 10.1016/j.epsl.2012.05.024.

Sonia M. Tikoo, Benjamin P. Weiss, William S. Cassata, David L. Shuster, J??r??me Gattacceca, Eduardo A. Lima, Cl??ment Suavet, Francis Nimmo, and Michael D. Fuller. Decline of the lunar core dynamo. *Earth and Planetary Science Letters*, 404:89–97, 2014. ISSN 0012821X. doi: 10.1016/j.epsl.2014.07.010.

Nicolas P. Walte, Giulio F.D. Solferino, Gregor J. Golabek, Danielle Silva Souza, and Audrey Bouvier. Two-stage formation of pallasites and the evolution of their parent bodies revealed by deformation experiments. *Earth and Planetary Science Letters*, 546:116419, 2020. ISSN 0012821X. doi: 10.1016/j.epsl.2020.116419. URL https://linkinghub.elsevier.com/retrieve/pii/S0012821X20303630.

John T. Wasson and Byeon-Gak Choi. Main-group pallasites: Chemical composition, relationship to IIIAB irons, and origin. *Geochimica et Cosmochimica Acta*, 67 (16):3079–3096, 2003. ISSN 00167037. doi: 10.1016/S0016-7037(03)00306-5. URL http://www.sciencedirect.com/science/article/pii/S0016703703003065.

Quentin Williams. Bottom-up versus top-down solidification of the cores of small solar system bodies: Constraints on paradoxical cores. *Earth and Planetary Science Letters*, 284(3-4):564–569, 2009. ISSN 0012821X. doi: 10.1016/j.epsl.2009.05.019. URL http://dx.doi.org/10.1016/j.epsl.2009.05.019.

Jijin Yang, Joseph I Goldstein, and Edward R D Scott. Iron meteorite evidence for early formation and catastrophic disruption of protoplanets. *Nature*, 446 (7138):888–91, apr 2007. ISSN 1476-4687. doi: 10.1038/nature05735. URL http://www.ncbi.nlm.nih.gov/pubmed/17443181.

Jijin Yang, Joseph I. Goldstein, and Edward R.D. Scott. Main-group pallasites: Thermal history, relationship to IIIAB irons, and origin. *Geochimica et Cosmochimica Acta*, 74(15):4471–4492, aug 2010. ISSN 00167037. doi: 10.1016/j.gca.2010.04.016. URL http://linkinghub.elsevier.com/retrieve/pii/S0016703710002012.